

## Interfacial roughness and related growth mechanisms in sputtered W/Si multilayers

T. Salditt, D. Lott, T. H. Metzger, and J. Peisl

*Sektion Physik der Ludwig-Maximilians-Universität München, Geschwister-Scholl-Platz 1, 80539 München, Germany*

G. Vignaud

*European Synchrotron Radiation Facility, Boîte Postale 220, 38043 Grenoble, France*

P. Høghøj and O. Schärpf

*Institut Lane-Langeuin, Boîte Postale 156, 38043 Grenoble, France*

P. Hinze and R. Lauer

*Physikalisch-Technische Bundesanstalt, Bundesalle 100, 38116 Braunschweig, Germany*

(Received 4 December 1995; revised manuscript received 2 May 1996)

We have studied interfacial roughness in amorphous W/Si multilayers grown by rf sputtering at different deposition parameters by cross-sectional transmission electron microscopy, x-ray reflectivity, and diffuse x-ray scattering. The diffuse scattering intensity has been recorded in an unprecedented wide range of parallel momentum transfer,  $5 \times 10^{-4} \text{ \AA}^{-1} \leq q_{\parallel} \leq 1 \text{ \AA}^{-1}$ , giving access to the height-height self- and cross-correlation functions on lateral length scales between a few  $\text{\AA}$  and  $1 \mu\text{m}$ . The results are compared for the different samples and discussed in view of the deposition parameters. [S0163-1829(96)02632-X]

### I. INTRODUCTION

Periodic multilayers of alternating high and low  $Z$  materials with periodicities  $d$  in the nanometer range have been studied extensively in recent years.<sup>1</sup> They are technologically important as soft x-ray mirrors,<sup>2-8</sup> with possible applications in the domain of x-ray microscopy, x-ray astronomy, and x-ray lithography, and as hard x-ray monochromators. More generally, multilayers are used for optical, magnetic, and electronic devices. The performance often depends crucially on the interfacial roughness so that the optimization of the growth process in this respect and the characterization of the roughness has become an important task. From a theoretic point of view the evolution of interfacial roughness during thin film growth is an interesting nonequilibrium process that has stimulated a lot of analytical and numerical work commonly known as the theory of kinetic roughening.<sup>9-11</sup>

The statistical properties of interfacial roughness in multilayer systems can be characterized by height-height correlation functions  $c_{ij}(r) = \langle h_i(\mathbf{r}'')h_j(\mathbf{r}') \rangle$ , where  $\langle \rangle$  denotes an ensemble average.  $h_i(\mathbf{r})$  is the deviation of the  $i$ th interface from its average position, and  $r = |\mathbf{r}'' - \mathbf{r}'|$  is the lateral distance between two positions  $\mathbf{r}'$  and  $\mathbf{r}''$ . In the case  $i=j$  correlations in one interface are described (*self-correlation function*), while  $i \neq j$  refers to correlations between different interfaces (*cross-correlation function*). Using a fundamental scaling hypothesis the asymptotic behavior predicted by kinetic roughening theory is of the form  $c_{ii}(r) \propto A - Br^{2H}$  for  $r \ll \xi$ , with the constants  $A$ ,  $B$  and the static roughness exponent  $H$ . Its value is limited to the range  $0 \leq H \leq 1$ , where for  $H=0$  the asymptotic law is to be replaced by a logarithmic correlation function  $c_{ii}(r) = A - B \ln(r)$ .<sup>9,11</sup> The correlation length  $\xi$  is a measure for the largest lateral interface structures and is expected to grow with time according to  $\xi \propto t^{1/z}$ . The values of  $H$  and of

$z$  specify the universality class of the growth process. At constant average growth velocity the total film thickness is proportional to time, so that the cross correlations  $c_{ij}(r)$  in a multilayer can be derived from the temporal propagation of roughness.<sup>12</sup> An important parameter of these cross-correlation functions is the vertical correlation length  $\xi_{\perp}$ . For long-range interface fluctuations  $\xi_{\perp}$  is generally larger than for fluctuations of small wave vector  $q_{\parallel}$ . The functional dependence of  $\xi_{\perp}(q_{\parallel})$  can be investigated by diffuse x-ray scattering.

A lot of efforts have been made in recent years to characterize buried interfaces quantitatively by different methods of x-ray scattering. Whereas the average density profile along the interface normal can be determined from x-ray reflectivity measurements, diffuse x-ray scattering away from the specular position can reveal information on lateral interface quantities like the correlation length and the roughness exponent of a self-affine interface or more generally the height-height correlation functions.<sup>13-16</sup> However, in practice, the determination of the correlation functions is only reliable if the reciprocal space is probed over a sufficiently large range<sup>17,18</sup> and with sufficiently high resolution. Here, we present diffuse scattering data in an unprecedented large range of parallel and normal momentum transfer,  $q_{\parallel}$  and  $q_z$ , respectively. The data have been partly recorded with a Si(220) analyzer crystal as has become feasible for diffuse scattering at the highly brilliant undulator x-ray source of the new European Synchrotron Radiation Facility (ESRF).<sup>19</sup> A typical data set covers a range of  $q_{\parallel}$  between  $5 \times 10^{-4}$  and  $1 \text{ \AA}^{-1}$ , giving access to the interface roughness on lateral length scales between a few  $\text{\AA}$  and  $1 \mu\text{m}$ . The method used to measure the diffuse x-ray scattering and to evaluate the data is a refinement of an approach reported recently.<sup>20</sup> In particular, the range of reciprocal space probed has been increased considerably both in  $q_{\parallel}$  and  $q_z$ . At the same time, the

TABLE I. Deposition parameters for samples A–F.

Sample	A	B	C	D	E	F
Ar pressure ( $10^{-3}$ mbar)	3.3	5.3	20	5.1	5.1	5.1
Bias voltage (V)	0	0	0	0	+30	-30
Sputter power Si (W)	500	500	500	750	750	750
Sputter power W (W)	750	750	750	1000	1000	1000

resolution in  $q_{\parallel}$  has been improved. Furthermore, two different methods of determining the self-correlation functions have been employed to prove the validity of the data evaluation. But apart from methodological improvements, the aim of this work is to compare the interfacial roughness (including both the rms roughness  $\sigma$  and the asymptotic behavior of the correlation functions) of several samples grown at different parameters. This is important to confirm the significance of a previous study<sup>20</sup> where the roughness of a magnetron sputtered W/Si multilayer was found to coincide well with the Edwards-Wilkinson growth model.<sup>21</sup>

The interfacial roughness in six amorphous W/Si multilayer samples of 60 bilayers with nominal periodicities around  $d \approx 80$  Å has been studied. The samples were grown on silicon wafers by rf-sputter deposition at different Ar pressures and different bias voltages at the substrate. Thus change in roughness that is well known to appear at Ar pressures above the thermalization threshold<sup>22</sup> as well as the changes associated with a bias voltage at the substrate<sup>23</sup> can be captured quantitatively.

The paper is organized as follows. The sample deposition is briefly described in Sec. II along with the characterization by x-ray reflectivity and cross-sectional transmission electron microscopy (TEM). Section III reports on the diffuse x-ray scattering experiment, while the data evaluation is presented in Secs. IV and V for the cross- and self-correlation functions, respectively. Finally, Sec. VI presents the discussion and a summary of the results.

## II. SAMPLE DEPOSITION AND CHARACTERIZATION

The multilayers were deposited by rf sputtering on commercial silicon (110) wafers with a diameter of 4 in. The wafers were covered by native oxide. Each sample consists of 60 W/Si bilayers with a nominal periodicity  $d \approx 80$  Å. The top layer was always silicon. Sample A was grown at a relatively low Ar pressure of about  $p_{\text{Ar}} = 3.5 \times 10^{-3}$  mbar, sample B at  $p_{\text{Ar}} = 5.3 \times 10^{-3}$  mbar, and sample C at  $p_{\text{Ar}} = 20 \times 10^{-3}$  mbar. The sample substrates were electrically isolated for samples A–D, while a dc bias voltage of +30 and -30 V was applied for samples D and E, respectively. Samples D–F were deposited at  $p_{\text{Ar}} = 5.1 \times 10^{-3}$  mbar. The rf power for the W and Si cycles was at about 50 and 750 W, respectively, for samples A, B, and C. For samples D, E, and F it was about 750 and 1000 W. The deposition parameters are summarized in Table I.

For sample C at  $p_{\text{Ar}} = 20 \times 10^{-3}$  mbar the system is above the thermalization threshold, where the mean free path of the incident target atoms becomes comparable to the distance of 6 cm between target and substrate. Thus the atoms impinge no longer ballistically with a small angular distribution of

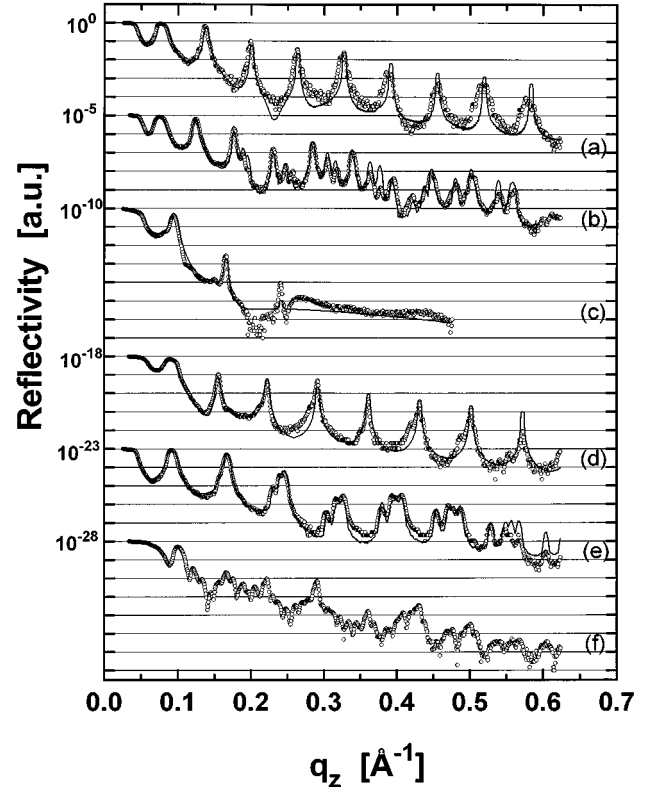


FIG. 1. Reflectivity curves of samples (a) A, (b) B, (c) C, (d) D, (e) E, and (f) F (circular data points) with the corresponding simulated curves (solid lines).

velocities, but from a random direction and with much less kinetic energy, since they have been thermalized by collisions with Ar atoms. Both effects, the distribution of incidence angles and the average energy, affect the growth mechanism.<sup>22</sup> A high amount of kinetic energy may enhance the diffusion length and provide activation energy for various aggregation processes. It may also result in a resputtering of atoms that are bound at energetically less favorable growth sites. Energy can be transported by sputtered target atoms as well as by Ar neutrals that are reflected from the target in charge exchange collisions.<sup>23</sup>

The thermalization transition has been previously studied for the systems Nb/Si,<sup>22</sup> Mo/Si,<sup>23</sup> and Nb/Al<sub>2</sub>O<sub>3</sub>.<sup>24</sup> In the case of Mo/Si the authors estimate the average energy deposited on the substrate by incoming adatoms to be of about 150 and 10 eV, for the Mo and Si atoms, respectively, if the Ar pressure is below the thermalization value, but only 60 and 2 eV, respectively, if it is above.

The six samples were first characterized by x-ray reflectivity at a 60-kW Rigaku rotation anode machine. A Ge(111) channel-cut monochromator was used to select Cu  $K\alpha_1$  radiation corresponding to a divergence of about  $\Delta\alpha_i \approx 0.007^\circ$ . Details on the reflectivity measurements, including the correction of the diffuse background with the corresponding *longitudinal diffuse* or *offset scans* and the *rocking scans* are reported elsewhere.<sup>25</sup>

The reflectivity curves are presented in Figs. 1(a)–1(f) as a function of the perpendicular momentum transfer  $q_z$ , for the samples A–F, respectively. Also shown are simulated

curves (solid lines) that have been calculated by the standard Parratt algorithm<sup>27</sup> taking roughness into account according to Nénot and Croce.<sup>28</sup> The parameters of layer thickness, mass density, and interface roughness are chosen in order to obtain a reasonable agreement between the data and the model. The limited resolution due to divergence and sample curvature has been taken into account. However, the fitting procedure is a formidable task for such a relatively high number of parameters. Various alternative parameter sets of similar quality can be found.<sup>25</sup> This drawback does not affect the periodicity  $d$  which can be determined with a precision of less than 1 Å, but it does result in relatively high error margins for values of the sublayer thickness  $d_{\text{Si}}$  and  $d_{\text{W}}$ , the electron density  $\rho_{\text{Si}}$  and  $\rho_{\text{W}}$ , as well as the rms roughness  $\sigma_{\text{Si}}$  and  $\sigma_{\text{W}}$ . All of the latter parameters collectively determine the amplitude of the reflectivity Bragg peaks.<sup>26</sup> The simulations correspond to  $\rho_{\text{Si}}=2 \text{ g/cm}^3$  and  $\rho_{\text{W}}=16 \text{ g/cm}^3$ . The rms roughness is kept constant throughout the stack for the sake of simplicity, even though it is believed that the value of  $\sigma$  increases from the bottom to the top. Thus the results for  $\sigma$  have to be regarded as somewhat averaged values that indicate the order of magnitude and can be taken to compare between different samples. Systematic errors at high reflectivity angles  $\alpha$  originate from the fact that fluctuations in the periodicity  $d$  are not included in the simulated model. These fluctuations cause a broadening of the higher-order Bragg peaks<sup>29</sup> that is not captured by the simulation. However, it can be evaluated independently by measuring the width of the peaks.

The reflectivity of Bragg peaks has been evaluated by normalizing their maximum count rates to the region of total external reflection. The normalization can experimentally be complicated mainly by two effects: sample illumination and sample curvature. However, given the large sample diameters and a beam size of 0.3 mm, the highest value of  $\alpha$  that was affected by a changing illumination was still well below the critical angle  $\alpha_c$  of total external reflection. On the other hand, the reflectivity profile at low angles  $\alpha$  of large samples is more susceptible to curvature, which ranked between 0.008 and 0.03  $\text{m}^{-1}$  (mean Gaussian curvature) as determined by optical Michelson interferometry.<sup>25</sup> To correct for this effect, the reflectivity profile at small angles was measured with several different detector slit openings to assure that all of the reflected intensity was captured. Sample curvature at angles well above  $\alpha_c$  was increasingly irrelevant. The same was true for the diffuse scattering experiment due to the small beam size of the undulator source (see Sec. III). The following observations can be made in Fig. 1.

(a) Sample A exhibits 14 pronounced Bragg peaks at angles of up to  $q_z \approx 0.85 \text{ \AA}^{-1}$ . The first Bragg peak has a reflectivity of 84% and is clearly broadened by dynamic scattering. The higher orders are split up into satellites, indicating some structural disorder in the bilayer periodicities. The diffuse background as measured with an offset angle of  $\omega=0.2^\circ$  is relatively low, more than three orders below specular at the position of the first Bragg peak and still about one order below specular at the 14th Bragg peak. The simulated curve corresponds to the parameters [ $d_{\text{Si}}=68.5 \text{ \AA}$ ,  $\sigma_{\text{Si}}=2.5 \text{ \AA}$ ;  $d_{\text{W}}=28.5 \text{ \AA}$ ,  $\sigma_{\text{W}}=5 \text{ \AA}$ ] $\times 60$ .

(b) The reflectivity curve of sample B shows a relatively slow intensity decay with  $q_z$  and a relatively complicated

pattern of peaks. The reflectivity of the first Bragg peak is 82% with a diffuse background about twice as high as for sample A. Beyond the third-order Bragg peak many more peaks are observed than expected for a uniform periodicity. Indeed, this behavior can be reproduced by the simulation assuming four multilayer stacks each of 15 bilayers with periodicities  $d=114, 113, 106, \text{ and } 102.5 \text{ \AA}$ , from the bottom to the top with an additional  $\text{SiO}_2$  cap layer of 15 Å thickness and density  $2.65 \text{ g/cm}^3$ . The rms roughness was at  $\sigma=3 \text{ \AA}$  throughout. However, alternative simulations show that neither the sequence of the four stacks nor the exact number of bilayers in each stack lead to significant changes in the quality of the fit.

(c) The profile of sample C is strikingly different: A decay of almost seven orders of magnitude over a range of only  $q_z \approx 4-5 q_{z,c}$ , with  $q_{z,c}$  denoting the critical  $q_z$  value of total external reflection followed by a broad ridge at  $q_z \geq 0.25 \text{ \AA}^{-1}$ . The latter is clearly specular but does not stem from the multilayer structure. The reflectivity of the first Bragg peak is as low as 40%. The diffuse background as measured with an offset angle of  $\omega=0.2^\circ$  was about two orders of magnitude below specular at the first Bragg peak, but only about a factor of 1.4 below specular at the third Bragg peak. Any attempt to obtain a reasonable fit over the whole range has failed. The solid line corresponds to a simulation of [ $d_{\text{Si}}=43 \text{ \AA}$ ,  $\sigma_{\text{Si}}=13 \text{ \AA}$ ;  $d_{\text{W}}=37 \text{ \AA}$ ,  $\sigma_{\text{W}}=16 \text{ \AA}$ ] $\times 60$  with a 40-Å-thick  $\text{SiO}_2$  layer of density  $2.5 \text{ g/cm}^3$  and rms roughness of equally 13 Å on top. Despite the unsatisfactory fitting, a periodicity of  $d=80 \text{ \AA}$  and an average interface roughness of about 15 Å can be deduced.

(d) The reflectivity profile of sample D shows well-formed Bragg peaks that indicate a quite homogeneous periodicity of  $d=88 \text{ \AA}$ . The 70% reflectivity of the first Bragg peak is lower and the intensity decay is slightly larger, as compared to samples A and B. The diffuse background level is similar to sample B. The simulated profile corresponds to [ $d_{\text{Si}}=37 \text{ \AA}$ ,  $\sigma_{\text{Si}}=3 \text{ \AA}$ ;  $d_{\text{W}}=51 \text{ \AA}$ ,  $\sigma_{\text{W}}=6 \text{ \AA}$ ] $\times 60$ . The difference in  $\sigma$  for the two sublayers is striking, but again one must be cautious as far as the significance of rms-roughness values is concerned, since the higher Bragg peaks are too large for the simulated curves, indicating that  $\sigma_{\text{Si}}$  has been chosen too small. However, a simulation with larger values leads to a disagreement between data and model in between the first four Bragg peaks.<sup>25</sup>

(e) Sample E shows the highest reflectivity of about 85% at the first Bragg sheet and a diffuse background that is about five times larger than that of sample A. The intensity decay is moderate. The third- and higher-order peaks split up into four satellites. This is modeled in the simulated curve by assuming four stacks with 15 bilayers each of different periodicities  $d=77.5, 79, 80.2, \text{ and } 83.2 \text{ \AA}$ . The sublayer thickness values are  $d_{\text{Si}}=0.74d$  and  $d_{\text{W}}=0.26d$ . The rms-roughness values are  $\sigma_{\text{Si}}=3 \text{ \AA}$  and  $\sigma_{\text{W}}=4.5 \text{ \AA}$ . Additionally, a 25-Å-thick  $\text{SiO}_2$  layer of density  $2.2 \text{ g/cm}^3$  and 3-Å rms roughness is assumed at the sample surface. Of course, details like the sequence of the different stacks cannot be relied on, but the discrete fluctuations in the  $d$  values are significantly evidenced by the simulation.

(f) The reflectivity curve of sample F shows a moderate intensity decay with an awkward pattern of relatively small peaks. The maxima cannot be attributed unambiguously to

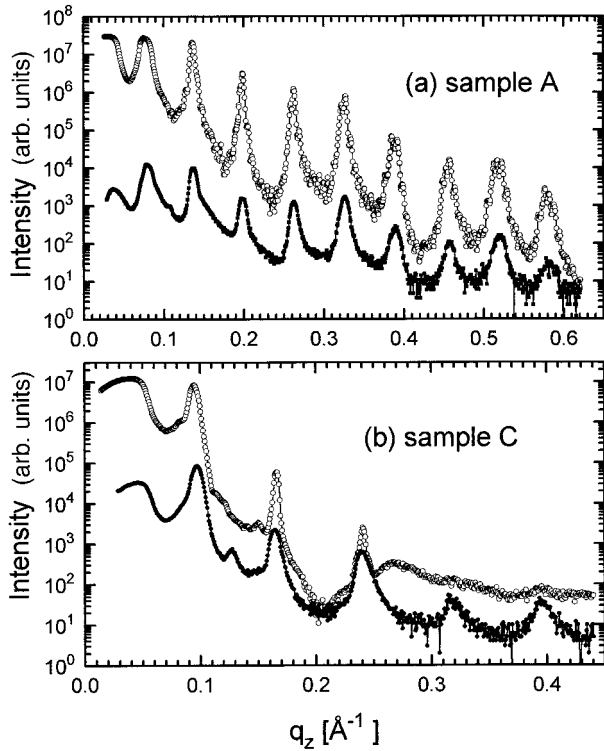


FIG. 2. Reflectivity curves (open circles) of samples (a) A and (b) C, with the corresponding longitudinal diffuse scans (solid circles) recorded at an offset angle  $\omega = \alpha_f - \alpha_i = 0.2^\circ$ . The diffuse intensity is scaled with respect to the specular curve according to monitor count rate and rocking scans. The lines are a guide to the eye.

subsequent orders of Bragg peaks, indicating a strong spatial disorder without a well-defined periodicity. Any attempt to simulate this curve without a detailed knowledge of the different layer spacings must fail. Eventually, some more information could be revealed by a Fourier inversion method. However, for the purpose of studying the interfacial roughness, this sample is not appropriate and will not be analyzed any further. In fact, by transmission electron microscopy it can be seen that sample F is composed of a series of multilayer stacks with drastically different periodicities. The results of the reflectivity fits are summarized in Table II.

To illustrate the ratio between specular and diffuse scattering along the specular path, the two extreme cases of samples A and C are presented in Figs. 2(a) and 2(b), respectively. The specular intensities (open circles) are shown

TABLE II. Parameters obtained from the fits of the reflectivity curves. Average values are given for samples with thickness fluctuations.

Sample	A	B	C	D	E	F
Layer thickness $d_{\text{Si}}$ ( $\text{\AA}$ )	68.5	78.5	43	37	59	
Layer thickness $d_{\text{W}}$ ( $\text{\AA}$ )	28.5	30	37	51	21	
Bilayer thickness ( $\text{\AA}$ )	97	118.5	80	88	80	
rms roughness $\sigma_{\text{Si}}$ ( $\text{\AA}$ )	2.5	3	13	3	3	
rms roughness $\sigma_{\text{W}}$ ( $\text{\AA}$ )	5	3	16	6	4.5	
Reflection of first Bragg peak (%)	84	82	40	70	85	50

along with the longitudinal diffuse scans (filled circles) with the proper scaling as determined from rocking scans and monitor normalization.<sup>25</sup> The offset angle was  $\omega = 0.2^\circ$ . The case of sample A is typical also for samples B, D, and E, indicating an almost negligible contribution of diffuse scattering, that decreases on average (apart from the Bragg-like peaks) with a power in between  $q_z^{-3}$  and  $q_z^{-2.5}$ .<sup>25</sup> Contrarily, the diffuse background in sample C is much more prominent, and decreases with a power in between  $q_z^4$  and  $q_z^{4.5}$ . It also exhibits the fourth and fifth Bragg-like peaks, which are covered by a broad intensity ridge in the specular curve. At these higher values of  $q_z$  the diffuse intensity is dominated by the rough W/Si interfaces, particularly in the top and center part of the stack, while the specular intensity might be determined mainly by the interfaces Si/SiO<sub>2</sub>, SiO<sub>2</sub>/W, as well as the first few Si/W interfaces.

The cross-sectional TEM measurements have been performed after a standard sample preparation with a Philips TEM CM 200 FEG microscope at a voltage of 200 kV with magnifications ranging between  $4.2 \times 10^4$  and  $8 \times 10^5$ . Atomic resolution was reached as proved by the crystal lattice of the Si substrate. For the standard technique of sample thinning and preparation we refer to Ref. 30. In the Si and W layers no indications of crystallites were found except for very small clusters in the Si layers of sample A. However, wide-angle x-ray data obtained in the geometry of grazing incidence diffraction shows the typical broad maxima of the amorphous structure factor.

Here, for the sake of brevity, only two micrographs of each moderate and high resolution are presented in Fig. 3 for [(a),(b)] sample E and [(c),(d)] sample C. Figure 1(a) covers nearly the whole multilayer stack of sample E from the substrate to the surface, while Fig. 1(b) shows the substrate and the first bilayer in high resolution. In Fig. 1(c) a micrograph of the first 24 bilayers of sample C are presented, and in Fig. 1(d) again the corresponding micrograph of the substrate and the first bilayer. Sample E shows a well-ordered multilayer stack with sharp interfaces, while for sample C lateral fluctuations of the interfaces are observed with a pronounced cumulative roughness in the first several periods that results in a columnar structure above. The network of columns separated by cusps resembles the results of previous publications on other multilayer systems.<sup>22,31</sup> Concerning the roughness, a quantitative comparison between x-ray reflectivity and TEM is difficult since the TEM pictures represent an interface position averaged along the path of the electrons. Hence lateral fluctuations can still be present, even if the interfaces seem very flat on the TEM micrographs, as is the case for all samples except for C. Furthermore, the individual layer thickness cannot be deduced from the TEM micrographs if the contrast function is not known. However, any fluctuations of the multilayer periodicity  $d$  can easily be detected by TEM, and compare well with the reflectivity result. In this respect, samples A and D are the best samples, with a relative thickness error  $\Delta d/d$  of  $\pm 2\%$ . These values are obtained from the high-order Bragg peaks that are slightly split on a logarithmic scale. Samples E and B are less perfect with a discrete set of deviations from the average periodicity (see above) of  $\pm 3\%$  and  $\pm 5\%$ , respectively, while for sample F bilayers are observed that differ in  $d$  by almost a factor of 2. More details on the TEM results in particular concerning the

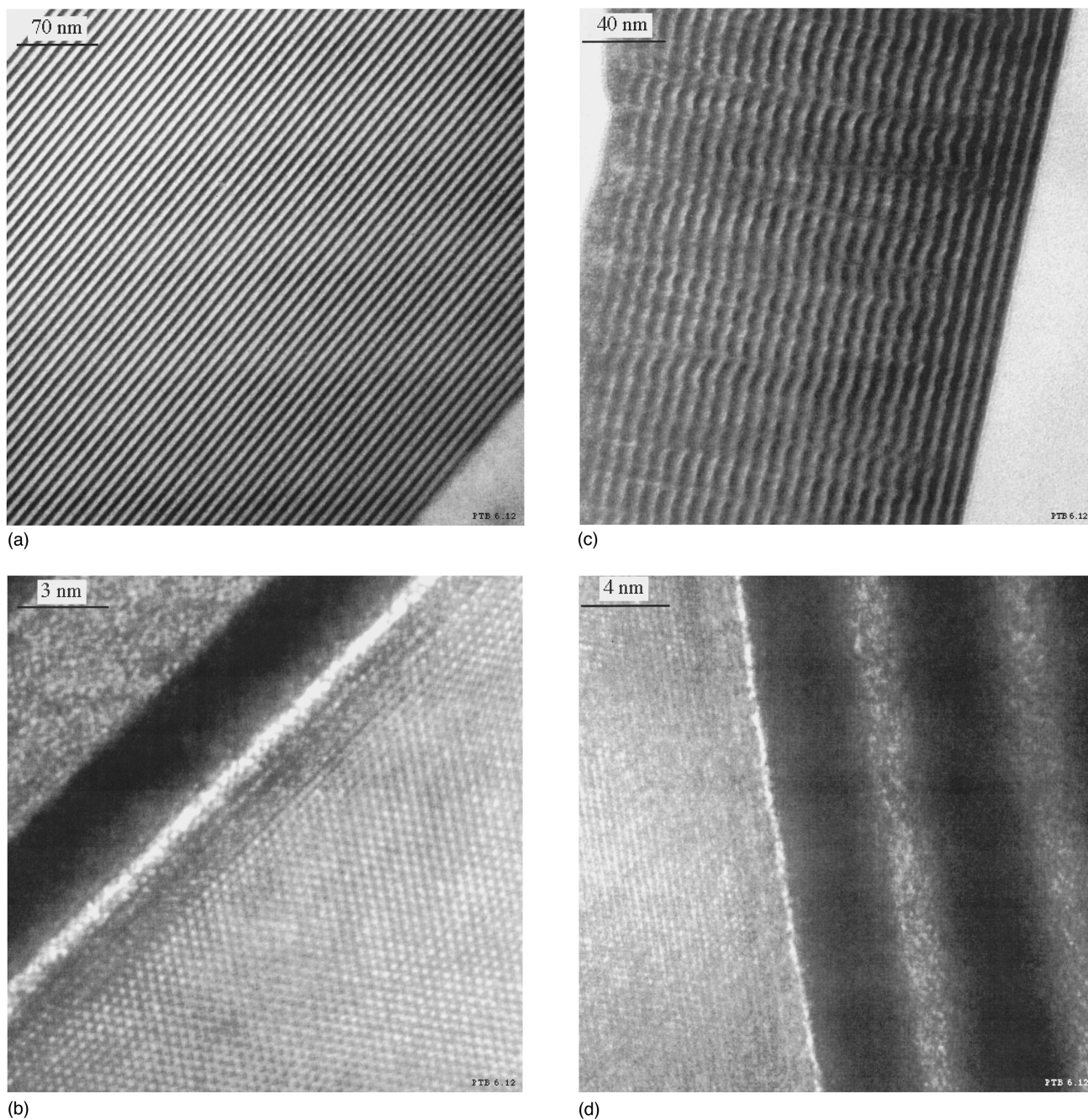


FIG. 3. TEM micrographs of [(a),(b)] sample E and [(c),(d)] sample C. The micrographs (a) and (c) cover the respective multilayer stacks over many periods starting from the substrate in moderate resolution, while (b) and (d) show the substrate and the first bilayer in high resolution. Note the respective scale bars.

high-resolution measurements can be found in Ref. 25.

The intent to study the effect of a negative bias voltage at the substrate is flawed by the poor quality of sample F, since it lacks a well-defined periodicity. The differences in thickness fluctuations between the different samples cannot be attributed to the growth conditions (Ar pressure, bias voltage). Instead, it occurred independently as a result of an error in the feedback system of the rf power, the result of which was made obvious by this study. In the meanwhile, after changing to a magnetron sputtering system, the quality and reliability of sample deposition has been greatly improved. For samples A, C, D, and E the thickness fluctuations also

exceeded the aim of  $\Delta d/d \leq 1\%$ . However, this did not impose a limit to the evaluation of the height-height correlation function, since (a) the lower diffuse Bragg sheets are not very sensitive to moderate thickness fluctuations, and (b) the scattering depth for the diffuse scattering experiment was typically restricted to about the ten top bilayers, see the next section.

### III. DIFFUSE SCATTERING

Diffuse (or *nonspecular*) x-ray scattering is a suitable method to probe roughness correlations in multilayers, since

the diffuse intensity distribution is uniquely determined by the correlation functions  $c_{ij}(r)$  provided no other density fluctuations are present.<sup>32</sup> In Born approximation the corresponding structure factor is given by<sup>14</sup>

$$S(\mathbf{q}) = \frac{L_x L_y}{q_z^2} \sum_{i,j}^N \Delta\rho_i \Delta\rho_j e^{-(1/2)q_z^2(\sigma_i^2 + \sigma_j^2)} e^{-iq_z(h_i - h_j)} \times \int dx \int dy (e^{iq_z^2 c_{ij}(r)} - 1) e^{-i(q_x x + q_y y)}, \quad (1)$$

where  $N$  is the total number of interfaces,  $\sigma_i$  the rms roughness of the  $i$ th interface,  $\Delta\rho_i$  is the contrast in scattering density, and  $L_x L_y$  the illuminated area.  $\mathbf{q} = (q_x, q_y, q_z) = \mathbf{k}_i - \mathbf{k}_f$  is the scattering vector, with the  $xy$  plane oriented parallel to the interfaces and the  $x$  direction in the plane of incidence. The mean surface normal points along the  $z$  direction. As can be deduced from Eq. (1), in a periodic multilayer the existence of cross correlations gives rise to an intensity modulation along the perpendicular momentum transfer  $q_z$  with peaks at the positions of  $q_z = n 2\pi/d$ , the so-called diffuse *Bragg sheets* or *diffuse Bragg-like peaks*.<sup>6</sup> Equation (1) has to be modified if the angles of incidence or exit  $\alpha_{i,f}$  are close to the critical angle  $\alpha_c$  of total external reflection, a condition for which refraction effects have to be taken into account by replacing the normal momentum transfer  $q_z$  in the vacuum by  $q'_z$  in the medium. Furthermore, in this case the Fresnel transmission functions modify the diffuse intensity, giving rise to the so-called Yoneda peaks at  $\alpha_{i,f} = \alpha_c$ .<sup>13,33</sup>

Apart from the correlation functions  $c_{ij}(r)$  the intensity distribution is also determined by the propagation of the incident and scattered wave field in the multilayer stack. Under the condition that the incidence or exit angle equals a Bragg angle of the specular reflectivity curve,  $\alpha_{i,f} = \alpha_n = \arcsin(n\lambda/2d)$ , multiple reflections at the interfaces add up coherently to form standing waves of periodicity  $d$  (Ref. 34) giving rise to resonant peaks and cusps in the diffuse scattering.<sup>35</sup> This dynamical effect can be employed to deduce selective information on the roughness of the  $A/B$  and  $B/A$  interface, respectively.<sup>36</sup> To account for both refraction effects and the dynamical propagation of the unperturbed wave field, a more general scattering theory has been derived in the framework of the distorted-wave Born approximation.<sup>15,16</sup> If however, the measurements are recorded with  $\alpha_{i,f} \neq \alpha_c$ , multiple reflections can be neglected and the diffuse scattering can be treated in the much easier kinematic approximation of Eq. (1), with  $q_z$  replaced by  $q'_z$  at low angles.

The depth sensitivity and selectivity of diffuse or *non-specular* x-ray scattering is determined by the scattering depth  $\Lambda$ . If  $\Lambda$  is much smaller than the multilayer periodicity  $d$  only the surface is probed, while in the opposite case the diffuse scattering of the top  $N \approx \Lambda/d$  periods is measured. The experimental control of  $\Lambda$  is achieved via refraction and absorption effects by an appropriate choice of the angles of incidence  $\alpha_i$  and exit  $\alpha_f$ , as is well known from grazing incidence diffraction.<sup>37</sup> The conventional scattering geometries used for measuring diffuse scattering (the so-called *rocking scan*, *detector scan*, and *offset scan*) are all restricted to the plane of incidence and thus do not allow one to record

data while keeping  $\alpha_i$  and  $\alpha_f$  constant. Thus the scattering depth may vary throughout the scan. As a consequence, the scattered intensity stems from a changing number of interfaces and the amount of signal will vary accordingly. Furthermore, the conventional scattering geometries suffer from a small accessible range in the parallel momentum transfer  $q_{\parallel} = (q_x^2 + q_y^2)^{1/2}$ .<sup>17</sup> These deficiencies can be overcome by measuring the diffuse scattering out of the plane of incidence,<sup>20,17</sup> where the detector is moved around an axis normal to the surface by an angle  $2\theta$  at constant  $\alpha_i$ ,  $\alpha_f$ , and thus constant  $\Lambda$ , i.e., the angle between the projections of  $\mathbf{k}_i$  and  $\mathbf{k}_f$  onto the surface is  $180^\circ - 2\theta$ , e.g., see Fig. 1 of Ref. 20. In this scattering geometry there is practically no upper limit of the  $q_{\parallel}$  range, hence the structure factor of the rough interfaces can be measured over a wide range of lateral length scales.

However, in the out-of-plane setup the resolution in  $q_{\parallel}$  ( $2\theta$ ) is considerably lower than in the conventional geometries.<sup>17</sup> To solve this problem we have used an asymmetric Si(220) analyzer crystal with the plane of diffraction oriented perpendicular to the plane of incidence, achieving a resolution in  $2\theta$  of about  $0.0013^\circ$ . The experimental setup is discussed in detail in Ref. 19. The experiment has been performed at the undulator beamline Troika of the ESRF in Grenoble. The beamline is located at a high  $\beta$  section of the 6-GeV storage ring at the ESRF and has a source size of  $970 \mu\text{m}$  [horizontal full width at half maximum (FWHM)] and  $210 \mu\text{m}$  (vertical FWHM) and a divergence of  $36 \mu\text{rad}$  (horizontal FWHM) and  $17 \mu\text{rad}$  (vertical FWHM), leading to a beam size of about  $1.8 \text{ mm}$  (horizontal) and  $1.1 \text{ mm}$  (vertical) at the position of the diamond(111) monochromator  $44.2 \text{ m}$  behind the source.<sup>38</sup> The monochromator was operated in  $35.5^\circ$  asymmetric Laue geometry, with an acceptance of  $\Delta\lambda/\lambda = 3.6 \times 10^{-5}$  centered around  $\lambda = 1.354 \text{ \AA}$ . The beam size at the sample was set by slits to about  $0.08 \text{ mm}$  in the vertical direction and  $1 \text{ mm}$  in the horizontal direction yielding typical footprints on the sample of  $4\text{--}9 \times 1 \text{ mm}^2$ , depending on  $\alpha_i$ . Higher harmonics [diamond(333) at  $\approx 27 \text{ keV}$ ] were suppressed by a Si mirror between the monochromator and the sample.

The diffuse scattering was alternatively measured by two detector arms rotating in the horizontal plane ( $2\theta$ ). On the first arm a goniometer with an  $18^\circ$  asymmetric Si(220) analyzer crystal was installed to record data of high resolution close to and in the plane of incidence ( $2\theta \leq 0.12^\circ$ ), with an acceptance angle of  $0.0013^\circ$  on the side oriented towards the sample. The one-dimensional position sensitive detector (gas-filled proportional counter) was oriented vertically, parallel to the  $2\theta$  rotational axis. The detector could also be mounted on a second detector arm at a distance of about  $70 \text{ cm}$  behind the sample with an evacuated flight tube of  $52 \text{ cm}$  length between the detector and the collimation slits (typically at  $2 \text{ mm}$ ). This setup was used to measure the diffuse intensity at higher angles  $2\theta \geq 0.2^\circ$ , where a resolution of  $0.09^\circ$  is sufficient. A better resolution would cause an intensity problem due to the strong decay of the structure factor with increasing  $q_{\parallel}$ .

Figure 4 shows the intensity distribution of sample A along  $\alpha_f$  at constant  $\alpha_i = 0.7^\circ$  as measured with the one-dimensional detector in the low-resolution setup at angles of  $2\theta = 0.2^\circ, 0.3^\circ, 0.4^\circ, 0.5^\circ, 0.6^\circ, 0.7^\circ, 0.8^\circ, 1.0^\circ, 1.5^\circ, 2^\circ, 3^\circ$ ,

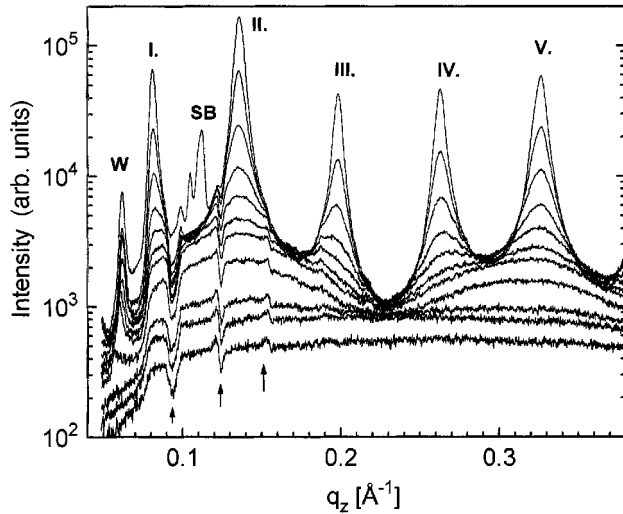


FIG. 4. The decay of the Bragg sheets in the range  $2\theta \geq 0.2^\circ$ , as measured in the low-resolution setup. From top to bottom curves corresponding to increasing angles of  $2\theta = 0.2^\circ, 0.3^\circ, 0.4^\circ, 0.5^\circ, 0.6^\circ, 0.7^\circ, 0.8^\circ, 1.0^\circ, 1.5^\circ, 2.0^\circ, 3.0^\circ, 5.0^\circ$  have been combined according to their relative intensities. The orders of the Bragg sheets are indicated by roman numbers and the specularly reflected beam by SB. The arrows indicate positions where the exit angle fulfills the conditions  $\alpha_f = n\alpha_{\text{Bragg}}$ .

and  $5^\circ$  (curves from top to bottom). The different curves are scaled by the correct intensity decay with  $2\theta$ . At  $2\theta = 0.2^\circ$  tails of the specularly reflected beam (SB) are still observed, due to the relatively low resolution of  $\Delta 2\theta = 0.09^\circ$ . One can further observe the first Bragg sheet (I) (nearly coinciding with the Yoneda maximum at  $\alpha_f = \alpha_c$ ) and four more Bragg sheets (II–V), which decay quickly with increasing  $2\theta$ . The scattering depths  $\Lambda$  corresponding to the Bragg sheets are  $\Lambda = 930, 1150, 1260, \text{ and } 1320 \text{ \AA}$ , respectively. The peak indicated by the letter W occurs at  $\alpha_f = 0$  and is probably due to a waveguide effect. The increase in the FWHM of the Bragg sheets with  $2\theta$  reflects the decline of the cross correlations for roughness fluctuations of smaller wavelength.<sup>20</sup> At  $2\theta \geq 0.7^\circ$  the corresponding cross-correlation length has become smaller than a bilayer (single layer or less) resulting in a change of periodicity along  $q_z$  and finally a flat intensity profile for  $2\theta \geq 1.5^\circ$ . Only the modulations due to dynamic effects indicated by the arrows remain. They occur at positions of  $\alpha_f$  equal to the first, second, and third Bragg angles of the specular reflectivity curve.

Similar data sets in high and low resolution have been recorded for samples B–E, which will be analyzed in the following two sections. For all samples, two main features are observed. First, the intensity decreases continuously with  $2\theta$ , corresponding to the decay of the structure factor  $S(q_{\parallel})$ . This decay reflects the in-plane correlations of the interfacial roughness and will be analyzed in Sec. V. Second, as described above for sample A, the modulations along  $\alpha_f$ , i.e., along  $q_z$  become weaker with increasing  $q_{\parallel}$ , i.e., the Bragg sheets become broader and finally vanish. Compared to the other samples, sample C shows a relatively strong decay of  $S(q_{\parallel})$ , with modulations along  $q_z$  that persist to particularly high values of  $q_{\parallel}$ , indicating a larger vertical correlation length even at small lateral length scales. It also exhibits a

much stronger decay of the diffuse intensity with  $q_z$ . The scattering depth corresponding to the first Bragg sheet is  $\Lambda = 900 \text{ \AA}$ .

For the sake of brevity, the corresponding data plots of samples B–F are not displayed here. The complete data are compiled in Ref. 25. Samples D and E show curves similar to sample A. Sample B exhibits satellite peaks for the Bragg sheets of third and higher orders reflecting the relatively large discrete thickness fluctuations, as discussed in the preceding section. Finally, sample F shows very broad modulations that can hardly be identified as Bragg sheets. The amount of continuous thickness fluctuations is so large that the multilayer can no longer be regarded as a periodic structure. This sample will therefore not be further analyzed in the following sections, since the data evaluation scheme relies on a well-defined periodicity. It consists of two parts aiming at the cross- and the self-correlation functions, respectively. For the latter, an integration of diffuse intensity over one multilayer “Brillouin zone”  $2\pi/d$  is required. If remnants of the specular peak are present in the Brillouin zone at low  $q_{\parallel}$ , they have to be cut away in the data treatment to sample exclusively the diffuse scattering. In the scattering geometry used, this is not a source of significant errors, since  $\alpha_i$  was selected to lay in between the Bragg sheets,<sup>19,25</sup> see Fig. 4.

The peak heights of different orders of Bragg sheets depend on the individual layer thicknesses, in a similar way as the positions of atoms in the elementary cell of a crystal determine the strength of Bragg reflections. The intensity distribution along  $q_z$  and the increasing width of the Bragg sheets is to be analyzed in the next section to obtain information on the cross-correlation functions.

#### IV. CROSS-CORRELATION FUNCTIONS

In this section the diffuse intensity distribution along  $q_z$  at constant  $2\theta$  is considered, e.g., the intensity-versus- $(q_z)$  curves displayed in Fig. 4. At large enough values of  $2\theta$  the variation of  $q_x$  in the abscissa of these curves is small compared to the  $q_y$  component so that the curves can be regarded nearly as at constant  $q_{\parallel}$ . We will try to explain the functional behavior by the simplest possible model that still captures the essential information on the cross-correlation functions that are to be deduced.

Let us assume that  $|q_z\sigma|^2$  is small enough to expand the exponential in Eq. (1). For a self-affine surface with  $c(r) = A - Br^{2H}$ ,  $0 < H < 1$ , the range of validity is given by  $|q_z\sigma|^2 \leq 1/H$  at  $q_{\parallel} = 0$ .<sup>39</sup> Correspondingly, the intensity is nearly constant for small  $|q_z\sigma|^2$  but falls off by a power law with an exponent  $2 + 2/H$  for high normal momentum transfer.<sup>13,17</sup> Accordingly, the intensity distribution can then be described by

$$S(\mathbf{q}) \propto \sum_{i,j}^N \Delta\rho_i \Delta\rho_j e^{-iq_z(h_i - h_j)} s_{ij}(\mathbf{q}), \quad (2)$$

$$s_{ij} = \int dx \int dy c_{ij}(r) e^{-i(q_x x + q_y y)}.$$

Furthermore, let us assume that the self-correlation functions are the same for all interfaces probed, i.e., that the roughness has become stationary. Of course, in a growth process this is

not the case at early times, but suppose that we probe only the top ten out of 60 bilayers. Then the increment in  $\sigma$  and  $\xi$  will not be so dramatic and average values should be sufficient to explain the data. Besides, if  $q_{\parallel}$  is large, the roughness will be probed on small length scales where it may indeed already have become stationary.

We now specify  $s_{ij}$  to be of the form

$$s_{ij} \propto s(q_{\parallel}) \exp(-\nu q_{\parallel}^2 |h_i - h_j|), \quad (3)$$

where  $s(q_{\parallel})$  is the Fourier transform of the self-correlation function (or spectral power density) and  $\nu$  is the so-called relaxation coefficient, which is inversely proportional to a  $q_{\parallel}$ -dependent (vertical) decay length of the cross correlations. For  $s(q_{\parallel}) = 1/(2\nu q_{\parallel}^2)$  Equation (2) represents the stationary solution of the so-called Edwards-Wilkinson equation.<sup>21,11</sup> In this simple model, a linear Langevin equation is taken to model the spatial and temporal behavior of a growing surface in the co-moving coordinate system,

$$\frac{\partial h(\mathbf{r}, t)}{\partial t} = \nu \nabla^2 h(\mathbf{r}, t) + \eta(\mathbf{r}, t), \quad (4)$$

where  $\eta$  is a Gaussian white noise term taking account of the random variations in the adatom flux, and  $t$  denotes the time or the film thickness, if a Galilei transformation  $t \rightarrow vt$  with a constant mean growth velocity  $v$  is applied. Assuming that the interface morphology stays in a metastable configuration, the model can be applied to the case of multilayers with different relaxation parameters for the individual sublayers, e.g.,  $\nu_{Si}$  and  $\nu_W$ .<sup>12</sup> In the limit of small gradients, the deterministic part of the equation  $\nu \nabla^2 h$  is proportional to the local curvature. In the so-called Mullins equation it is replaced by  $\nu \nabla^4 h$ ,<sup>40,11</sup> leading to a corresponding change in the interface dynamics, i.e.,  $q_{\parallel}^2$  is replaced by  $q_{\parallel}^4$  in Eq. (4). Combinations of such linear terms in the equation would also be possible, leading to different interface dynamics.<sup>41</sup> The Edwards-Wilkinson equation is the linear version of the more general Kardar-Parisi-Zhang equation that has an additional nonlinear term proportional to  $(\nabla h)^2$ .<sup>42</sup> This nonlinear term can vanish intrinsically for some models. For others it may be only relevant at asymptotically long times (or large thicknesses) depending on the prefactors of the linear and the nonlinear terms, respectively. In these cases the Edwards-Wilkinson equation is a good candidate to model the growth.

Equation (2) is now taken to simulate the intensity distribution. The values of  $d_{Si}$ ,  $d_W$ ,  $\nu_{Si}$ ,  $\nu_W$ ,  $\rho_{Si}$ ,  $\rho_W$ , and an absorption coefficient are the parameters that enter. Additionally, before comparing to experimental data,  $q_z$  has to be transformed into  $q'_z$  to account for refraction. Finally a normalization constant is employed for each  $q_{\parallel}$ . However, the number of free fit parameters is much smaller. Since the thickness values, the densities, the absorption coefficient, and the critical angle have to coincide with the reflectivity measurements or theoretical values (absorption), at least within the limit of the error bars, only the scaling factor and the two relaxation parameters are to be varied. One can additionally restrict the model to  $\nu_{Si} = \nu_W$  since the detail of eventual differences in the two sublayers will not become evident except at very high  $q_{\parallel}$ , see below.

A fit of the intensity distribution of sample A at  $2\theta = 0.2^\circ$  is shown in Fig. 5(a) (solid line) as a function of normal

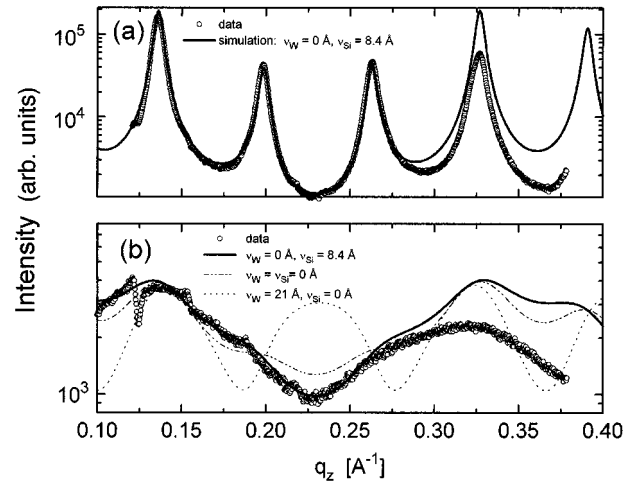


FIG. 5. Sample A: diffuse intensity as a function of  $q_z$  at (a)  $2\theta = 0.2^\circ$  and (b)  $2\theta = 0.8^\circ$  (open circles), as well as the respective simulations (solid lines).

momentum transfer  $q_z$  on a logarithmic scale. The data (open circles) are those of the topmost curve in Fig. 4. The parameters of the simulation are  $\text{Im}(q_z) = 0.0011$ ,  $\nu_{Si} = 8.4 \text{ \AA}$ , and  $\nu_W = 0 \text{ \AA}$ . The simulated curve has been adjusted with a constant background and an open scaling parameter. It describes the data points very well up to  $q_z \approx 0.3 \text{ \AA}^{-1}$ ; from there on it is systematically too high. However, this deviation is to be expected since the approximation of small roughness was used without taking the intensity decay with  $q_z$  into account.<sup>17</sup> Any effort to improve this will rely on assumptions on the self-correlation function. The peak heights of the Bragg sheets are very sensitive to the individual layer thickness  $d_{Si}$  and  $d_W$ , analogous to the dependence of Bragg reflections on the positions of atoms in the elementary cell of a crystal. Thus a valuable check of the reflectivity results is possible. In contrast, the simulation is not very sensitive to the individual relaxation parameters, as long as the average relaxation parameter of one bilayer  $\nu = (d_{Si}\nu_{Si} + d_W\nu_W)/d$  is the same. This is plausible, since the corresponding vertical correlation length is still much larger than the bilayer thickness  $\xi_{\perp} \ll d$ .

In Fig. 5(b) the same procedure is applied to the intensity distribution at  $2\theta = 0.8^\circ$ . The data are again taken from the set of curves displayed in Fig. 4. Here, the periodicity of the  $q_z$  modulation has changed to a larger value corresponding to a smaller distance in real space. This phenomenon occurs at  $\xi_{\perp} \leq d$ , when the interfaces separated by more than  $d$  are no longer correlated and the diffuse scattering does not add up with a fixed phase relationship. However, the correlation across one sublayer may still be appreciable, so that the modulation along  $q_z$  will reflect a sublayer thickness. In the general case, a superposition of modulations corresponding to both sublayers will be observed, weighted by the respective degree of cross correlation, which is governed by both the thickness and relaxation parameters. Three simulations with different sets of  $\nu_{Si}$ ,  $\nu_W$ , yet with the same average relaxation  $\nu$  are plotted:  $\nu_{Si} = 8.4 \text{ \AA}$ ,  $\nu_W = 0 \text{ \AA}$  (solid line),  $\nu_{Si} = 0 \text{ \AA}$ ,  $\nu_W = 21 \text{ \AA}$  (dotted line), and  $\nu_{Si} = \nu_W = 6 \text{ \AA}$  (dash-dotted line). Clearly, the only model that can explain the data (apart from the dynamic cusp at  $q_z = 1.22 \text{ \AA}^{-1}$  and the systematic deviation at high  $q_z \sigma$ ) is one with  $\nu_W \approx 0$  and all of

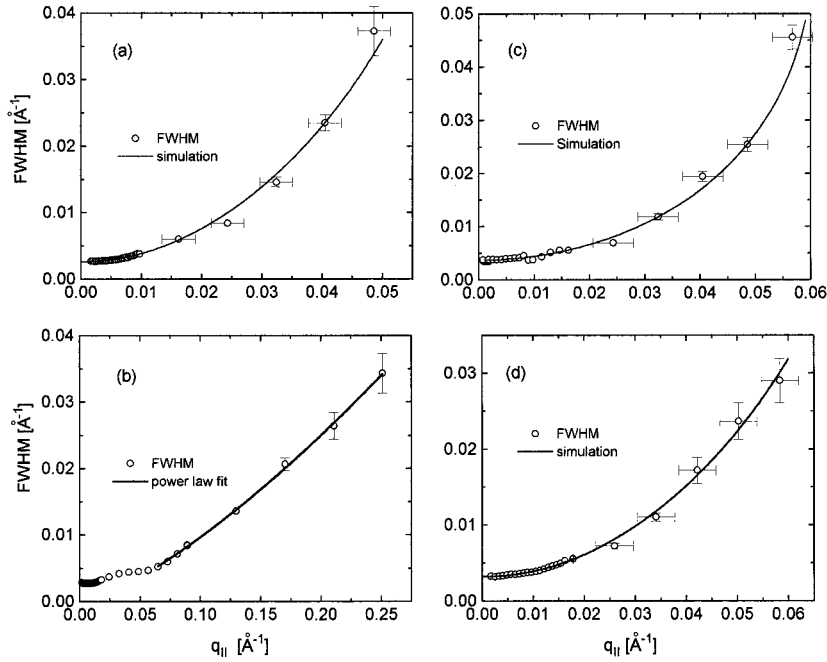


FIG. 6. The Bragg sheet width as a function of  $q_{\parallel}$  for (a) sample A, (b) sample C, (c) sample D, and (d) sample E.

the relaxation taking place during the growth of the Si sub-layer. This is an interesting result, since it indicates that the two interfaces are not identical. It implies that the Si/W interface is rougher than the W/Si one.

The fitting procedure outlined above can of course be applied to any curve at arbitrary  $q_{\parallel}$  for the whole sample set. However, this would be a very tedious and cumbersome procedure. Instead, the information that we are most interested in can be deduced in a much simpler way, where only the FWHM of the Bragg sheets as a function of  $q_{\parallel}$  is analyzed to determine the dependence of  $\xi_{\perp}$  on  $q_{\parallel}$ . In the case of a power-law relationship the corresponding exponent can be identified with the dynamic growth exponent,<sup>43</sup> e.g.,  $z=2$  for the Edwards-Wilkinson model. Of course, the cross-correlation length  $\xi_{\perp}$  is not the only quantity that can determine the width of the Bragg sheets. Even at infinite  $\xi_{\perp}$ , the Bragg sheet would have a finite width due to the finite number of interfaces, absorption, extinction (if dynamical effects are important), fluctuations of the periodicity  $d$ , or cumulative roughness.<sup>29</sup> However, the latter effects only influence the saturation value of the FWHM at low  $q_{\parallel}$  but do not change it as a function of  $q_{\parallel}$ . In other words they impose a minimum width, which can further be determined independently from the width of the specular Bragg peaks. Only in the case of dynamical broadening (generally only at the lowest- or lower-order Bragg peaks) can the FWHM of the specular curve be larger than of the corresponding diffuse Bragg sheet.

In Fig. 6(a) the FWHM of the second Bragg sheet of sample A is shown as a function of  $q_{\parallel}$  with the estimated error bars. The data points (open circles) are analyzed with a model simulation based on an exponential cross-correlation function with a cross-correlation length given by  $\xi_{\perp} \propto q_{\parallel}^{-z}$ . For  $z=2$  this reduces to the model used above. The solid line corresponds to the parameters  $\text{Im}(q_z)=0.0011 \text{ \AA}^{-1}$ ,  $\nu_{\text{Si}}=9 \text{ \AA}$ ,  $\nu_{\text{W}}=0 \text{ \AA}$ , and  $z=2$ . Hence there the data are in good agreement with the Edwards-Wilkinson model. However, the error in  $\Delta z = \pm 0.2$  is quite large. In contrast to sample A, the

width of the Bragg sheets of sample C is much smaller, indicating a higher cross-correlation length. Furthermore, the  $q_{\parallel}$  dependence of the Bragg sheet width is much weaker, see the FWHM of the first Bragg sheet in Fig. 6(b). Due to the limited scattering depth the width takes a constant value at  $q_{\parallel} \leq 0.025 \text{ \AA}^{-1}$ , before it increases slightly to a plateau around  $0.04 \text{ \AA}^{-1}$  and finally increases more rapidly for  $q_{\parallel} \geq 0.06 \text{ \AA}^{-1}$ . In this case a simple model with a uniform  $\xi_{\perp}(q_{\parallel})$  dependence cannot give the right answer. For  $q_{\parallel} \geq 0.06 \text{ \AA}^{-1}$  a power-law fit to the FWHM as a function of  $q_{\parallel}$  yields an exponent of 1.37 (solid line). In this range absorption can be neglected and we have thus equally  $z=1.37$ , since  $\xi_{\perp}$  is then simply inversely proportional to the cross-correlation length.

In Figs. 6(c) and 6(d), the FWHM of the second Bragg sheet is shown for samples D and E, respectively, together with the corresponding simulations. The simulation parameters were at (a)  $\text{Im}(q_z)=0.0016 \text{ \AA}^{-1}$ ,  $\nu_{\text{Si}}=4 \text{ \AA}$ ,  $\nu_{\text{W}}=3 \text{ \AA}$ ,  $z=2$ , and (b)  $\text{Im}(q_z)=0.00135 \text{ \AA}^{-1}$ ,  $\nu_{\text{Si}}=4 \text{ \AA}$ ,  $\nu_{\text{W}}=3 \text{ \AA}$ , and

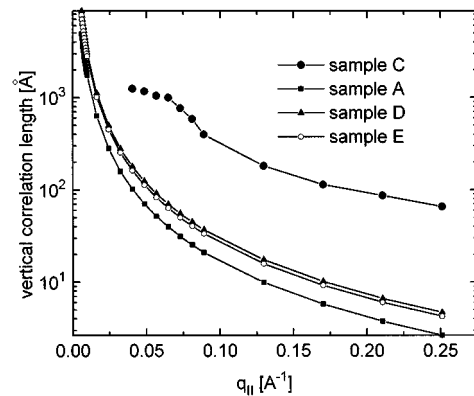


FIG. 7. Comparison between the vertical correlation lengths  $\xi_{\perp}$  of samples C, A, D, and E. For sample C sputtered at high Ar pressure the roughness is obviously much more conformal than for the samples sputtered at low pressure.

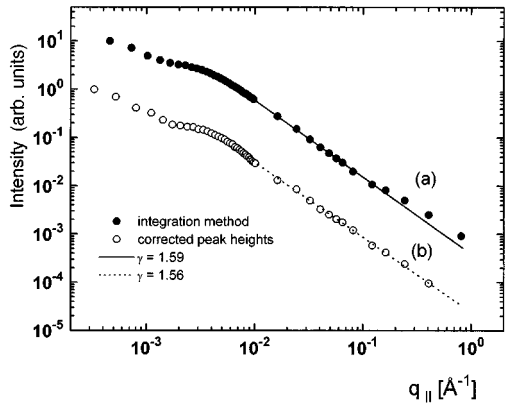


FIG. 8. Sample A: The intensity decay with  $q_{\parallel}$  as obtained by (a) integrating the intensity over one Brillouin zone centered around the second Bragg sheet as a function of  $q_{\parallel}$  on a double-logarithmic scale (filled circles) and (b) the same decay (open circles, shifted vertically for clarity) obtained from the corrected peak heights (see text). The solid and dotted lines represent power-law fits with respective exponents  $\gamma=1.59$  and  $1.56$ .

$z=2$ . Thus in both cases the data agree well with the Edwards-Wilkinson model. For sample B the evaluation of the FWHM was obscured by the prominent thickness fluctuations.

For comparison, in Fig. 7 the cross-correlation lengths  $\xi_{\perp}(r)$  as determined from the simulations are shown for samples (a) A, (b) C, (c) D, and (e) E, as a function of the lateral wave vector  $q_{\parallel}$ .

## V. SELF-CORRELATION FUNCTIONS

In this section the average height-height self-correlation function of the interfacial roughness is investigated. Consider a stack of layers all of equal thickness  $d$ . As can be shown from Eq. (2), the self-correlation function can be separated from the cross-correlation functions by integrating the diffuse intensity over one Brillouin zone  $\Delta q_z = 2\pi/d$  in reciprocal space.<sup>20</sup> By adding up the terms with indices  $i, j$  and  $j, i$  of the double sum, the identity  $c_{ij}(r) = c_{ji}(r)$  gives the factor  $\cos[q_z d(i-j)]$ , using the approximation  $\exp[-iq_z(h_i - h_j)] \approx \exp[-iq_z d(i-j)]$ . Due to the oscillatory behavior in  $q_z$  all terms with  $i \neq j$ , the cross correlations cancel and only the terms containing the self-correlation functions are summed up. One can then treat the resulting expression by an effective ‘‘one-interface’’ theory to obtain information on an average self-correlation function within the scattering depth  $\Lambda$ . In the following, this procedure will be called the *integration method*. In the case of two different sublayer thicknesses  $d_{S1} \neq d_W$  the situation is more complicated, but as long as the vertical correlation length is much larger than the bilayer thickness  $\xi_{\perp} \gg d$ , the diffuse intensity will again be modulated in reciprocal space with a periodicity of  $2\pi/d$ . Only if  $\xi_{\perp} \leq d$ , as can become possible for high-frequency fluctuations, will the pattern of intensity modulation change corresponding to the sublayer thickness, as discussed in the preceding section. In this case the integration method is no longer appropriate.

Figure 8(a) shows the intensity distribution of the second Bragg sheet of sample A as a function of  $q_{\parallel}$  recorded at

$\alpha_i = 0.7^\circ$ , with the intensity integrated over the second Brillouin zone  $3\pi/d \leq q_z \leq 5\pi/d$  (open circles). In the treatment of the raw data the effects of polarization, sample illumination, and monitor count rate have been considered. The shoulder of the curve at  $q_{\parallel} = 0.002 \text{ \AA}^{-1}$  and the change of slope at  $q_{\parallel} \approx 0.004 \text{ \AA}^{-1}$  could not have been resolved without analyzer crystal.<sup>19</sup> In the interval  $5 \times 10^{-3} \text{ \AA}^{-1} \leq q_{\parallel} \leq 5 \times 10^{-1} \text{ \AA}^{-1}$  the diffuse intensity can be approximated by a power law as expected for a self-affine interface. From a numerical fit (solid line) the exponent  $\gamma = 1.59$  is obtained. It should be pointed out that the deviation of the experimental data points from the straight line at large  $q_{\parallel}$  occurs exactly at those values of  $q_{\parallel}$  where the modulation along  $q_z$  changes its nature from the  $2\pi/d$  periodicity to a longer one, see, e.g., in Fig. 4. As discussed in the preceding section, the latter modulation corresponds to cross correlations of the two interfaces that border the  $W$  sublayers.

The relatively slow decay of the intensity with  $q_{\parallel}$  is in contrast to a static roughness exponent  $H > 0$ , for which the exponent of the structure factor is approximately given by  $\gamma = 2 + 2H$ .<sup>17</sup> For a logarithmic correlation function  $c(r) = A - B \ln(r)$  the exponent  $\gamma$  is given by  $\gamma = 2 - |q_z \sigma|^2 / 2$  if  $|q_z \sigma|^2 \leq 4$ ,<sup>13</sup> which could explain the data for  $\sigma = 7 \text{ \AA}$ . It is difficult to say whether this value is still within the error margin of the reflectivity result. However, a fit of the reflectivity curve with  $\sigma_W = 7 \text{ \AA}$  and  $\sigma_{S1} = 4 \text{ \AA}$  is not significantly worse than the one shown in Fig. 1(a). Thus a logarithmic correlation function is in agreement with the data. Furthermore, the scattering depth around the second Bragg sheet is limited to approximately the top ten bilayers, where cumulative roughness could result in a rms roughness that is larger than the average values determined from the reflectivity curve.

Further evidence for a logarithmic correlation function could be gathered by an investigation of the other Bragg sheets. However, the first Bragg sheet occurs at  $\alpha_f \approx \alpha_c$ , where the scattering depth  $\Lambda$  varies very rapidly from less than one bilayer to several bilayers and the integration method is somewhat ill defined. Furthermore, the simple Born approximation has to be replaced by distorted-wave Born approximation (DWBA) in this case. For the third-, fourth-, and fifth-order Bragg sheets the integration method leads to a decay with exponents between  $0.8 \leq \gamma \leq 1.1$ . As expected, the decay is weaker than for the second Bragg sheet. However, there are two problems to be considered. First, the formula  $\gamma = 2 - |q_z \sigma|^2 / 2$  obviously cannot be correct for orders higher than 3, since it would predict a constant diffuse intensity profile and eventually an increase with  $q_{\parallel}$  at  $|q_z \sigma|^2 \geq 4$ . Numerical simulations of a logarithmic correlation function show that the intensity profile becomes very flat at high  $|q_z \sigma|^2$  with no asymptotic regime reached within a range of  $q_{\parallel} \leq q_c$ , where  $q_c = 2\pi/a$  is a cutoff corresponding to the atomic next-neighbor distance  $a$ . Besides, if  $|q_z \sigma| \geq 1$  the length  $a$  has to be specified explicitly in the calculation of the integrand of Eq. (1) to avoid a divergence at small  $r$ . Thus a reliable evaluation of the higher-order Bragg sheets requires further theoretical investigations on the x-ray structure factor for logarithmic correlation functions.

The second problem is connected to the validity of the integration method, that becomes incorrect for high  $|q_z \sigma|^2$ , since the decay with  $q_{\parallel}$  might then be significantly different

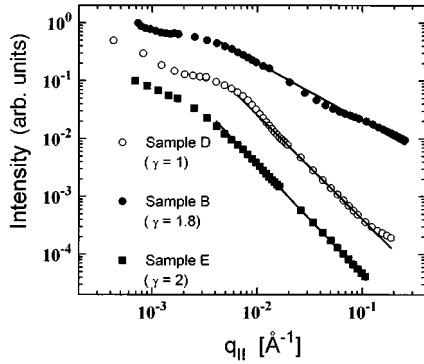


FIG. 9. Samples D, B, and E: The decay of the intensity integrated over one Brillouin zone centered around the second Bragg sheet as a function of  $q_{\parallel}$  on a double-logarithmic scale. The solid lines represent the corresponding power-law fits.

at the upper and the lower border of the Brillouin zone, respectively. The corresponding error depends on the width of the Bragg sheet.<sup>44</sup> To test the approximation in the case of the second Bragg sheet, an alternative method is used. The peak intensity of the second Bragg sheet is taken for each value of  $q_{\parallel}$  and divided by the function describing the intensity distribution along  $q_z$  at corresponding values of  $q_{\parallel} = (q_x^2 + q_y^2)^{0.5}$ . This function takes account of the changing peak height due to the cross correlations independent of any decay with  $q_{\parallel}$ . Thus once this function is known, i.e., by the fitting shown in Figs. 5(a) and 5(b), it only has to be factored out from the measured decay to obtain the average decay with  $q_{\parallel}$  that can be interpreted by a one-interface theory, i.e., the structure factor of the average interface. The result is shown in Fig. 8(b): a power-law decay over a range  $0.004 \text{ \AA}^{-1} \leq q_{\parallel} \leq 0.4 \text{ \AA}^{-1}$  with an exponent  $\gamma = 1.56 \pm 0.05$  that is well in agreement with the integration method ( $\gamma = 1.59$ ). The advantage is that in this case the data points at high  $q_{\parallel}$  are also described correctly. However, an accurate description of the intensity distribution as a function of  $q_z$  is necessary to apply this procedure.

The correlation length can be estimated from the onset of the power-law decay to be  $\xi \approx 2\pi/0.004 \text{ \AA}^{-1} \approx 1500 \text{ \AA}$ . The increase of the curve at  $q_{\parallel} \approx 0.001 \text{ \AA}^{-1}$  is not understood in the model of a logarithmic correlation function. It is present in all curves that extend to the corresponding low range of  $q_{\parallel}$ . Of course, it cannot be observed at the higher-order Bragg sheets where even at  $q_y = 0 \text{ \AA}^{-1}$  the component  $q_x = 2\pi/\lambda (\cos \alpha_f - \cos \alpha_i)$  is too large. Furthermore, this feature is also observed for samples B and D, proving the existence of a roughness component on lateral length scales of  $r \geq 5000 \text{ \AA}$  that must not necessarily be self-affine nor be due to the multilayer growth. Instead, it could stem from the substrate, since the Edwards-Wilkinson model predicts a cross-correlation length  $\xi_{\perp}$  well above the total multilayer thickness for these length scales, see curve, Fig. 7.

The behavior of sample C grown at high Ar pressure is significantly different. The onset of the power-law decay occurs at  $q_{\parallel} \approx 0.05 \text{ \AA}^{-1}$ , indicating a relatively low correlation length of about  $\xi \geq 150 \text{ \AA}$  in agreement with the TEM micrograph in Fig. 3(b). Besides, the intensity decay with  $q_{\parallel}$  is much stronger, about four orders of magnitude of diffuse intensity in the range  $q_{\parallel} \leq 1 \text{ \AA}^{-1}$ . The decay can be associated with an exponent  $H = 0.7$ , and thus differs significantly

from the behavior predicted by the Edwards-Wilkinson equation. We plan to publish the analysis along with eventual theoretical explanations of the corresponding growth mode after further investigation.<sup>45</sup>

Figure 9 shows the intensity decay with  $q_{\parallel}$  for the samples D, B, and E, shifted vertically for clarity. The top curve shows the decay of the intensity integrated around the second Bragg sheet for sample D at  $\alpha_i = 0.7^\circ$ . The data points do not coincide very well with a power law, but an average decay corresponding to  $\gamma \approx 1$  can be identified. This would be in agreement with a logarithmic self-correlation function with an average rms roughness  $\sigma = 7 \text{ \AA}$  and a value of  $\xi \approx 2\pi/0.004 \text{ \AA}^{-1} \approx 1600 \text{ \AA}$ .

The curve in the middle represents the integrated intensity of the second Bragg sheet of sample B. The intensity has been recorded at  $\alpha_i = 0.95^\circ$ . An exponent of  $\gamma = 1.8 \pm 0.1$  is determined from a least-squares fit. This is in agreement with a logarithmic self-correlation function, if the average rms roughness is in the range  $4 \text{ \AA} \leq \sigma \leq 7 \text{ \AA}$ , which is possible, especially since a cumulative roughness can lead to higher values at the top than the  $3\text{--}4 \text{ \AA}$  determined from reflectivity. The correlation length can be estimated to be  $\xi \approx 2\pi/0.007 \text{ \AA}^{-1} \approx 900 \text{ \AA}$ . The exponents obtained from the third- and fourth-order Bragg sheet are  $\gamma = 1.5$  and  $\gamma = 0.85$ , respectively, with the restrictions as discussed above.

Finally, the lowest curve shows the integrated intensity decay of the second-order Bragg sheet of sample E, as recorded at  $\alpha_i = 0.85^\circ$ . The data are described well by a power law of  $\gamma = 2.1 \pm 0.1$  in the range  $0.006 \text{ \AA}^{-1} \leq q_{\parallel} \leq 0.1 \text{ \AA}^{-1}$ . Assuming a rms roughness of  $\sigma = 3 \text{ \AA}$  a logarithmic correlation function would yield  $\gamma = 1.9$ . Smaller values of  $\sigma$  are not in agreement with the reflectivity curve. Thus there is more evidence for a roughness exponent  $0 \leq H \leq 0.1$ , which is still very close to logarithmic behavior. The correlation length can be estimated to be  $\xi \approx 2\pi/0.004 \text{ \AA}^{-1} \approx 1600 \text{ \AA}$ .

## VI. SUMMARY AND DISCUSSION

In summary, six W/Si multilayers deposited by rf sputtering at different Ar pressures and bias voltages have been investigated by x-ray reflectivity, transmission electron microscopy, and diffuse x-ray scattering. Reflectivity and TEM have revealed significant fluctuations of the bilayer periodicity ( $\Delta d \geq 10\%$ ) in two samples. Independent of the growth conditions they can be attributed to a deficiency in the feedback control of the rf power. X-ray reflectivity has further been used to determine the density, roughness, and thickness of the sublayers. However, due to the large number of parameters in the fitting procedure and the corresponding uncertainty in finding the proper minimum, rather large errors for these values are estimated.

The diffuse x-ray scattering intensity has been mapped in reciprocal space in a large range of parallel and perpendicular momentum transfer, which becomes possible in the scattering geometry of grazing incidence diffraction. Furthermore, this technique allows one to keep the scattering depth and hence the number of interfaces probed constant. Information on the height-height self-correlation functions of the interfaces was determined from the intensity distribution along the parallel momentum transfer  $q_{\parallel}$ , after integration along  $q_{\perp}$  over one Brillouin zone  $2\pi/d$ . All samples depos-

ited at Ar sputter gas pressures below the thermalization value (A, B, D, E) have shown a very slow power-law decay of the structure factor with  $q_{\parallel}$  corresponding to exponents between 1 and 2. This behavior is in contrast to self-affine interfaces with a static roughness exponent  $0 \leq H \leq 1$ , but can be explained by a logarithmic self-correlation function, similar to capillary waves. The correlation lengths for these samples are relatively large,  $\xi \geq 1000 \text{ \AA}$ .

Within the experimental errors, the cross-correlation length  $\xi_{\perp}$  for the samples grown at low Ar pressure decay as  $q_{\parallel}^{-2}$ . Both findings, the logarithmic self-correlation and the  $q_{\parallel}^{-2}$  dependence of the cross correlations are in agreement with the Edwards-Wilkinson model,<sup>21,11</sup> where the relaxation mechanism is induced by the local interface curvature. Alternative models could only explain the data if they predicted the same or similar self-correlations and cross correlations. By this we mean that the data could also be in agreement with a correlation function that falls off even weaker than a logarithmic correlation function, see Sec. V. Correspondingly, the dynamic exponent  $z$  could also be slightly larger than 2, see Sec. IV. However, any model with self-similar roughness of  $H$  larger than 0.1 is completely out of scope.

The sample sputtered above the thermalization value shows a completely different behavior. On the TEM micrograph a columnar structure is observed. The rms roughness is higher than in the other samples by a factor of 2 to 3. Here, the correlation length is relatively small and the power-law decay at high  $q_{\parallel}$  is much stronger. At the same time, the Bragg sheets persist to much higher  $q_{\parallel}$ , indicating strong cross correlations even on small lateral length scales. These findings indicate a completely different scaling behavior and hence growth mechanism than the Edwards-Wilkinson type. The main physical differences between the low and the high Ar regimes are the distribution of incidence angles of the adatoms and their kinetic energy. Postulating a resputtering mechanism that leads to desorption of adatoms on energeti-

cally less favorable growth sites, the Laplace term in the Edwards-Wilkinson equation [Eq. (4)] can be explained at low Ar pressure where the kinetic energy of the impinging atoms is roughly between 10 and 100 eV. This relaxational term must vanish if the kinetic energy of adatoms has been thermalized and desorption has become impossible.

In summary, the following somewhat simplified picture evolves for the amorphous W/Si multilayers studied here: a sample that is well suited for practical application is usually one which exhibits smooth interfaces with little roughness. In terms of height-height correlation functions these samples are characterized by a logarithmic self-correlation function. This is intuitively convincing, since in this case the mean height deviation  $g(r) = \langle h(\mathbf{r}'') - h(\mathbf{r}') \rangle = 2\sigma^2 - 2c(r)$  is proportional only to  $\ln(r)$  rather than a strong power-law increase with  $g(r) \propto r^{2H}$ . In the latter case even a relatively small correlation length  $\xi$  may yield a considerable rms roughness, e.g., for  $H > 0.5$ , while for the samples with logarithmic behavior a much longer correlation length along with a smaller rms roughness is observed. The cross correlations reflect the efficiency of the relaxation mechanism that is active during growth. For the better samples this relaxation or smoothening is governed by the local interface curvature, while in the opposite case no such mechanism is present, resulting in a very conformal roughness even for fluctuations of small lateral length scales.

#### ACKNOWLEDGMENTS

This work was supported by the Bundesministerium für Forschung und Technologie under Contract No. 055WMAXI5. The excellent research conditions provided by ESRF scientists, in particular by G. Grübel and J. LeGrand at the Troika beamline, are acknowledged. We further thank Ch. Lamers, H. Gleyzolle, D. Abernathy, and Z. Kovats for help with the experiment, and are indebted to M. Kardar and H. Spohn for helpful discussions.

- 
- <sup>1</sup> *Physics, Fabrication, and Applications of Multilayer Structures*, edited by P. Dhez and C. Weisbuch (Plenum, New York, 1987).
- <sup>2</sup> E. Spiller, D. Stearns, and M. Krumrey, *J. Appl. Phys.* **74**, 107 (1993).
- <sup>3</sup> D. E. Savage, J. Kleiner, N. Schimke, Y. H. Phang, T. Jankowski, J. Jacobs, R. Kariotis, and M. G. Lagally, *J. Appl. Phys.* **69**, 1411 (1991).
- <sup>4</sup> D. E. Savage, Y. H. Phang, J. J. Rownd, J. F. MacKay, and M. G. Lagally, *J. Appl. Phys.* **74**, 6158 (1993).
- <sup>5</sup> Y. H. Phang, D. E. Savage, T. F. Kuch, M. G. Lagally, J. S. Park, and K. L. Wang, *J. Appl. Phys.* **72**, 4627 (1992).
- <sup>6</sup> Y. H. Phang, D. E. Savage, R. Kariotis, and M. G. Lagally, *J. Appl. Phys.* **74**, 3181 (1993).
- <sup>7</sup> F. E. Christensen, A. Hornstrupp, and H. W. Schnopper, *Appl. Opt.* **27**, 1548 (1988).
- <sup>8</sup> D. G. Stearns, R. S. Rosen, and S. P. Vernon, *Appl. Opt.* **32**, 6952 (1993).
- <sup>9</sup> J. Krug and H. Spohn, in *Solids far from Equilibrium*, edited by C. Godrèche (Cambridge University Press, Cambridge, England, 1992).
- <sup>10</sup> P. Meakin, *Phys. Rep.* **235**, 191 (1994).
- <sup>11</sup> A. L. Barabási and H. E. Stanley, *Fractal Concepts in Surface Growth* (Cambridge University Press, Cambridge, England, 1995).
- <sup>12</sup> D. G. Stearns, *Appl. Phys. Lett.* **62**, 1745 (1993).
- <sup>13</sup> S. K. Sinha, E. B. Sirota, S. Garoff, and H. B. Stanley, *Phys. Rev. B* **38**, 2297 (1988).
- <sup>14</sup> S. K. Sinha, *J. Phys. (France) III* **4**, 1543 (1994).
- <sup>15</sup> V. Holý, J. Kubena, I. Ohlidal, K. Lischka, and W. Plotz, *Phys. Rev. B* **47**, 15 896 (1993).
- <sup>16</sup> V. Holý and T. Baumbach, *Phys. Rev. B* **49**, 10 668 (1994).
- <sup>17</sup> T. Salditt, T. H. Metzger, Ch. Brandt, U. Klemradt, and J. Peisl, *Phys. Rev. B* **51**, 5617 (1995).
- <sup>18</sup> T. Salditt, T. H. Metzger, J. Peisl, B. Reinker, M. Moske, and K. Samwer, *Europhys. Lett.* **32**, 331 (1995).
- <sup>19</sup> T. Salditt, D. Lott, T. H. Metzger, J. Peisl, G. Vignaud, J. F. Legrand, G. Grübel, P. Høghøj, and O. Schärpf, *Physica B* **221**, 13 (1996).
- <sup>20</sup> T. Salditt, T. H. Metzger, and J. Peisl, *Phys. Rev. Lett.* **73**, 2228 (1994).
- <sup>21</sup> S. F. Edwards and D. R. Wilkinson, *Proc. R. Soc. London, Ser. A* **381**, 17 (1982).

- <sup>22</sup>E. E. Fullerton, J. Pearson, C. H. Sowers, S. D. Bader, X. Z. Wu, and S. K. Sinha, *Phys. Rev. B* **48**, 17 432 (1993).
- <sup>23</sup>S. P. Vernon, D. G. Stearns, and R. S. Rosen, *Appl. Opt.* **34**, 6969 (1993).
- <sup>24</sup>T. Salditt, T. H. Metzger, J. Peisl, Ch. Morawe, and H. Zabel, in *Evolution of Thin-Film and Surface Structure and Morphology*, edited by B. G. Demczyk *et al.*, MRS Symposia Proceedings No. 355 (Materials Research Society, Pittsburgh, 1995), p. 269.
- <sup>25</sup>D. Lott, Diplomarbeit, LMU München, 1995.
- <sup>26</sup>P. Pershan, *J. Phys. Condens. Matter* **6**, A37 (1994), and references therein.
- <sup>27</sup>L. G. Parratt, *Phys. Rev.* **95**, 359 (1954).
- <sup>28</sup>L. Nénot and P. Croce, *Rev. Phys. Appl.* **15**, 761 (1980).
- <sup>29</sup>A. P. Payne and B. M. Clemens, *Phys. Rev. B* **47**, 2289 (1993).
- <sup>30</sup>N. G. Chew and A. G. Cullis, *Ultramicroscopy* **23**, 175 (1987).
- <sup>31</sup>D. J. Miller, K. E. Gray, R. T. Kampwirth, and J. M. Murduck, *Europhys. Lett.* **19**, 27 (1992).
- <sup>32</sup>M. Rauscher, T. Salditt, and H. Spohn, *Phys. Rev. B* **52**, 16 855 (1995).
- <sup>33</sup>D. K. G. de Boer, *Phys. Rev. B* **51**, 5297 (1995), and references therein.
- <sup>34</sup>J. B. Kortright, *J. Appl. Phys.* **61**, 1130 (1987).
- <sup>35</sup>X. Jiang, T. H. Metzger, and J. Peisl, *Appl. Phys. Lett.* **61**, 8 (1992); *Phys. Status Solidi B* **179**, 299 (1993).
- <sup>36</sup>S. K. Sinha, in *Neutron Scattering in Materials Science II*, edited by D. A. Neumann, T. P. Russell, and B. J. Wuensch, MRS Symposia Proceedings No. 376 (Materials Research Society, Pittsburgh, 1995).
- <sup>37</sup>H. Dosch, in *Critical Phenomena at Surfaces and Interfaces*, edited by G. Höhler, Springer Tracts in Modern Physics Vol. 126 (Springer, Berlin, 1992).
- <sup>38</sup>ESRF annual report, 1994 (unpublished).
- <sup>39</sup>M. Rauscher (private communication).
- <sup>40</sup>W. W. Mullins, *J. Appl. Phys.* **28**, 333 (1957).
- <sup>41</sup>W. M. Tong and R. S. Williams, *Annu. Rev. Phys. Chem.* **45**, 401 (1994).
- <sup>42</sup>M. Kardar, G. Parisi, and Y. C. Zhang, *Phys. Rev. Lett.* **56**, 869 (1986).
- <sup>43</sup>M. Kardar (private communication).
- <sup>44</sup>T. Salditt, Ph.D thesis, Universität München, 1995.
- <sup>45</sup>T. Salditt, D. Lott, T. H. Metzger, J. Peisl, P. Høghøj, O. Schärpf, R. Fischer, and J. Zweck (unpublished).